Multicycle activity of natural $CaCO_3$ minerals for Thermochemical Energy Storage in Concentrated Solar Power plants

Monica Benitez-Guerrero [1, 2], Jose Manuel Valverde [1], Pedro E. Sanchez-Jimenez [2], Antonio Perejon [2, 3], Luis A. Perez-Maqueda [2]*

[1] Facultad de Física, Universidad de Sevilla, Avenida Reina Mercedes s/n, 41012 Sevilla, Spain.

[2] Instituto de Ciencia de Materiales de Sevilla, C.S.I.C.-Universidad de Sevilla, C. Américo Vespucio nº49, 41092 Sevilla, Spain.

[3] Departamento de Química Inorgánica, Facultad de Química, Universidad de Sevilla, Sevilla 41071, Spain.

Abstract: Thermochemical energy storage in Concentrated Solar Power plants by means of the Calcium-Looping process is a promising novel technology that would allow for a higher share of renewables. A main benefit of this technology is the use of widely available, non-toxic and environmentally friendly calcium carbonate minerals as raw materials to store energy. Efficient integration of the Calcium-Looping process into Concentrated Solar Power plants involves the endothermic calcination of $CaCO_3$ in the solar receiver while the exothermic carbonation of CaO is carried out at high temperature under high CO_2 partial pressure. The heat released by this reaction is carried out by the excess CO_2 and employed for power generation by means of a closed CO_2 cycle. This works explores the multicycle Calcium-Looping performance of naturally occurring $CaCO_3$ minerals such as limestone, chalk and marble for thermochemical energy storage in Concentrated Solar Power plants. Despite their similar composition (almost pure $CaCO_3$), these minerals exhibit a significant difference in their Calcium-Looping multicycle activity, which may be attributed to differences in particle size and microstructure. Pore plugging at the Calcium-Looping conditions for thermochemical energy storage tested in our work is a main limiting mechanism on the multicycle CaO carbonation activity.

Keywords: Concentrated Solar Power, Thermochemical Energy Storage, Calcium Looping, limestone, chalk, marble

*Prof. Dr. J.M. Valverde
Facultad de Física, Universidad de Sevilla
Avenida Reina Mercedes s/n, 41012 Sevilla (Spain)
Tel +34 954550960 Fax +34 954239434
E-mail: jmillan@us.es

1 Introduction

Solar energy is one of the most promising sources of renewable energy as it is clean, abundant and cost-free. Moreover, Concentrated Solar Power (CSP) plants lend themselves to be integrated into the grid for large scale electricity generation (Hinkley et al., 2013) (Siva Reddy et al., 2013). However, to overcome the inherently intermittent nature of direct solar irradiation it is mandatory to develop massive energy storage technologies for power generation during prolonged periods. To this end, a number of *Thermochemical Energy Storage* (TCES) systems are being investigated as a more efficient alternative to energy storage in the form of sensible heat using molten salts as currently employed in commercial systems (Zhang et al., 2013) (Fernández et al., 2014). Among the main advantages of TCES systems we can find a potentially high energy density and the possibility of permanent storage without losses (N'Tsoukpoe et al., 2009) (Pardo et al., 2014). The high temperatures attainable in CSP plants with tower technology make it possible to achieve highly endothermic chemical decomposition reactions. In this context, the *Calcium-Looping* (CaL) process, which is based on the calcination/carbonation of $CaCO_3$,

$$\mathrm{CaO_{(s)} + CO_{2(g)} \rightleftarrows CaCO_{3(s)}} \qquad \Delta Hr^0 = -178\ \mathrm{kJ/mol} \qquad (1)$$

can be carried out at a fast rate in the temperature range typical of CSP plants with tower technology (above 700ºC). Scalability of the CaL process would be facilitated by its simplicity and the use of cheap (~ 10$/ton), abundant and non-toxic naturally occurring $CaCO_3$ minerals as raw materials (Prieto et al., 2016) (Chacartegui et al., 2016).

The idea of integrating the CaL process into CSP plants for energy storage dates back to the 1970s (Barker, 1973) (Barker, 1974) (Flamant et al., 1980), and has gained renewed interest in recent years (Pardo et al., 2014) (Chacartegui et al., 2016) (Cot-Gores et al., 2012). Briefly, once $CaCO_3$ particles are calcined by concentrated solar irradiation, the products of the reaction (CaO and CO_2) are stored separately. When needed, these byproducts are brought together at carbonation conditions to use the heat from this exothermic reaction to produce electricity. The flow diagram of a possible CaL-CSP integration, as recently proposed in (Chacartegui et al., 2016), is shown in Figure 1. The system comprises a heliostat field, a solar calciner, a carbonator, two reservoirs for CaO and $CaCO_3$ storage, a CO_2 compression-storage and a power unit. After calcination, the sensible heat of the reaction byproducts is recovered by heat exchangers before storing them separately. On demand, CaO and CO_2 are recirculated into the carbonator where the heat of the carbonation reaction is recovered and transported

to a gas turbine by the excess of CO_2 not intervening in the carbonation reaction. Thus, electricity is generated by means of a CO_2 closed cycle. CaL conditions leading to high global efficiencies in the CaL-CSP integration involve carbonation temperatures above 850ºC under high CO_2 partial pressure (Chacartegui et al., 2016). In addition, fast calcination at moderate temperatures would be desirable to use inexpensive metal based solar receivers (Ávila-Marín, 2011) (Behar et al., 2013). As seen in previous works, the use of helium in the calciner atmosphere would allow to achieve fast $CaCO_3$ calcination at temperatures as low as 700ºC (Sarrion et al., 2016) due to the high thermal conductivity of He and the extremely high diffusivity of the released CO_2 in this gas (Berger, 1927) (Cussler, 1997). Moreover, the CO_2/He mixture could be separated by using commercial membranes (Taketomo and Fujiura, 1984) for reutilizing both gases in the cycle.

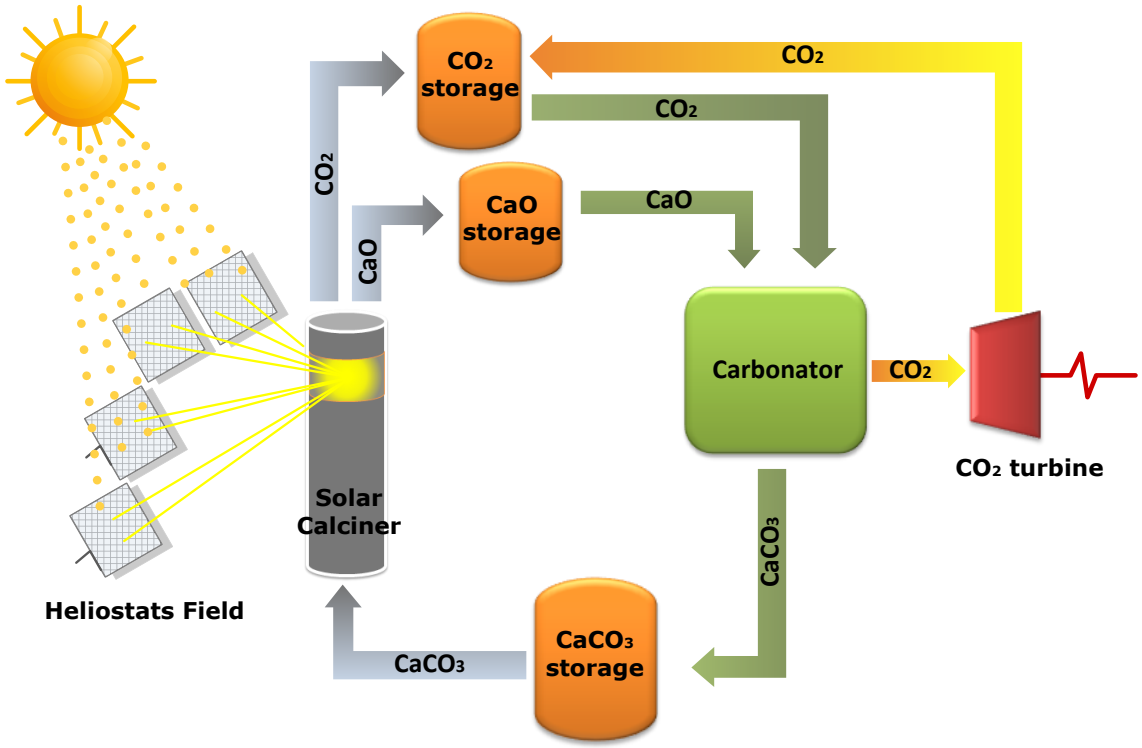

Figure 1. Flow diagram of the Calcium-Looping thermochemical energy storage system for concentrated solar power plants. A detailed description is found in (Chacartegui et al., 2016).

The CaL process has been widely investigated in the last years for its application to capture the CO_2 released by the combustion of fossil fuels (Stanmore and Gilot, 2005) (Blamey et al., 2010) (Cormos and Simon, 2015). The standard CaL process to capture CO_2, which has

been successfully demonstrated at the pilot-scale level (Perejón et al., 2016), employs lime (CaO) in a bed reactor (carbonator) at temperatures close to 650ºC fluidized by the post-combustion flue gas at atmospheric pressure and loaded with a relatively low CO_2 concentration (15% vol). After carbonation of CaO particles, they are circulated into a second fluidized bed reactor (calciner), where CaO is regenerated at high calcination temperatures (930-950ºC) under a high CO_2 concentration environment. Thus, CO_2 at high concentration is recovered from the calciner to be compressed and stored, and the regenerated CaO particles are recirculated to the carbonator to be used in a new cycle. Under these harsh calcination conditions, CaO particles are severely sintered, which causes CaO conversion to drop dramatically in just a few cycles. Remarkably, these CaL-CO_2 capture conditions are diverse from those specific of CaL-CSP storage above described.

Particle size is a relevant physical property for industrial applications, such as the CaL process, based on circulating fluidized beds (CFBs), where open cyclone exchangers are employed to recover the fine particles elutriated in the gas stream (Chacartegui et al., 2016) (Ebrahimi and Rahmani, 2016) (Lu et al., 2008). According to Barker (Barker, 1974), the carbonation/calcination reaction would be only reversible in short residence times for particles of size around 10 nm while the optimum size of particles to be used in CFBs is in the rage 100-500 μm (Dieter et al., 2013) (Arias et al., 2013) (Ströhle et al., 2014) (Hanak et al., 2015). For particles of size in this range, physical mechanisms such as intraparticle pore diffusion and pore plugging might limit significantly the reaction kinetics thus hampering the CaO multicycle activity as depending on reaction conditions (Grasa et al., 2008) (Alvarez and Abanades, 2005).

In general, most of the studies focused on the effect of particle size on CaO conversion have been carried out under CO_2 capture conditions. According to Abanades and Álvarez (Abanades and Alvarez, 2003) (carbonation at 650ºC under 20%CO_2; calcination at 900ºC in air) the multicycle CaO conversion decay is similar for particles of size in the range between 100 and 800 μm for limestone samples obtained from different sources. On the other hand, the study carried out by Grasa et al. (Grasa et al., 2008) (carbonation at 650ºC under P_{CO2} =0.01MPa; calcination at 850ºC in air/O_2), shows an increasing resistance to intraparticle CO_2 diffusion as particle size is increased in the range between 250 and 1000 μm. In another study using particle size fraction from 50 to 600 μm (carbonation at 650ºC under P_{CO2} =0.01MPa; calcination at 900ºC in air), it was concluded that the effect of particle size is almost negligible after the fourth carbonation cycle (Grasa et al., 2009). In a later work using particles of size in the range between 75 and 800 μm (carbonation close to calcination temperature under

100%CO_2; calcination at 880ºC under 0/100%air-50%CO_2/50%air), these same authors demonstrated that the calcination reaction is chemically controlled for particles sizes up to 300 μm, for which diffusional effects are considered negligible. For larger particles (600-800 μm), the calcination rate becomes slower due to both the internal resistance to CO_2 diffusion and hindered reaction kinetics (Martínez et al., 2012). Nonetheless, Li et al. (Li et al., 2009) observed that CaO conversion measured in a fixed-bed reactor (carbonation at 550-750ºC under 15%CO_2/85%N_2 – 100%CO_2; calcination at 920-1100ºC under 80%CO_2/20%O_2) decreased further with the number of cycles as the particle size of the starting limestone was increased in the ranges of less than 125 μm, 160-315 and 315-415 μm. Most of these researches are aimed at analyzing the effect of particle size on the multicycle CaO conversion under CO_2 capture conditions. However, the carbonation/calcination conditions employed are usually diverse especially in regards to the calcination stage, which could explain the contrasting results reported. In addition to operation conditions, the presence of oxides other than CaO may play a role on deactivation by either enhancing or mitigating CaO sintering. Thus, the presence of MgO together with CaO in dolomite is seen to improve significantly the CaO multicycle activity (Fennell et al., 2007) (Sun et al., 2008) (Beruto et al., 2010) (Coppola et al., 2013).

The majority of studies performed on Ca based natural minerals to be used in the CaL process are focused on limestone and dolomite with the goal of analyzing the behavior of these materials for CO_2 capture (Perejón et al., 2016) (Erans et al., 2016). Besides of limestone, other naturally occurring $CaCO_3$ minerals are marble and chalk, whose behavior is scarcely reported in the literature (Pacciani et al., 2010) (Wdowin et al., 2012) (Pinheiro et al., 2016). The present work is focused on analyzing the CaL performance of limestone, marble and chalk at conditions for CSP storage.

2 Materials and Methods

The natural calcium carbonate minerals analyzed in our work were limestone (Pedrera, Sevilla) supplied by Segura S.L., chalk (Arboç, Tarragona) and marble (Purchena, Almería), the latter two supplied by Omya Clariana.

The multicycle activity of the CaO derived from these natural carbonates was measured by using a Q5000IR thermogravimetric analyzer (TA Instruments) at CaL conditions for CSP storage. The instrument is provided with a high sensitivity balance (<0.1 μg) and a furnace heated by IR halogen lamps allowing for high heating/cooling rates up to 300ºC/min

and stable isotherms (<4ºC). A small mass of sample (10 mg) was used in all cases to prevent undesired mass transfer effects due to CO_2 diffusion resistance across the powder. Each run was started by a precalcination stage heating the sample from room temperature to 725ºC at 300ºC/min under a helium atmosphere. This calcination temperature was held for 5 min. Then, the temperature was increased (300ºC/min) to 850ºC and maintained during 5 min for carbonation under pure CO_2. After carbonation, the sample was calcined by decreasing the temperature (300ºC/min) to 725ºC and changing the gas to pure He. In a real fluidized bed calciner it can be expected that the CO_2 concentration will increase with height due to the released CO_2. This issue cannot be however replicated in a TGA apparatus and should be addressed in future fluidized bed tests. The calcination stage was kept for 5 min to achieve full CaO regeneration. Carbonation was carried out again by increasing the temperature (300ºC/min) to 850ºC and introducing pure CO_2 after which a new cycle was started. Between the calcination and carbonation stages an intermediate cooling stage was introduced by decreasing the temperature (100ºC/min) to 300ºC and keeping it for 2 min under He. The goal of this stage was to simulate in practice the extraction of sensible heat from the solids streams exiting the reactors before being stored. For comparison, CaL cycles at conditions for CO_2 capture were also performed. In these experiments, carbonation took place at 650ºC under 15% vol CO_2/85% vol air during 5 min whereas calcination was carried out at 950ºC under 70% vol CO_2/ 30% vol air for 5 min. Quick transitions between both stages were achieved by means of high heating/cooling rates (300ºC/min). A total of 20 carbonation/calcination cycles were performed in this way for each sample.

In addition to TGA tests, carbonation/calcination cycles were also performed in a separate tubular furnace to obtain samples of sufficient mass for porosimetry analysis. In this furnace, a 1 gram sample was subjected to a precalcination stage under N_2 for 90 min at 750ºC. CaO samples stemming from precalcination were labeled as **L_cal_1**, **C_cal_1** and **M_cal_1** meaning the CaO obtained after a first calcination for limestone, chalk and marble, respectively. The precalcined samples were also subjected to 5 carbonation/calcination cycles. **L_cal_6**, **C_cal_6** and **M_cal_6** samples refer to the CaO obtained after these cycles for limestone, chalk and marble, respectively. Carbonation/calcination conditions consisted of carbonation under pure CO_2 at 850ºC for 15 min and calcination under pure N_2 at 750ºC during 30 min. In all cases, the temperature ramp rates were 10ºC/min. Even though these conditions do not mirror exactly those used in the TGA tests, the characterization of the samples obtained from these tests serves to get a grip on the mechanism that limits the CaO multicycle activity when calcination is carried out under relatively low temperature at low CO_2 partial pressure

and the samples are carbonated at high temperature under pure CO_2, which are the main cornerstones of CSP storage conditions.

X-Ray fluorescence analysis was performed by means of an energy-dispersive X-ray instrument (Axios PW4400, PANalytical). X-ray powder diffraction measurements were carried out using a MiniFlex600 (Rigaku) with Ni filtered CuKα radiation (λ = 1.5406 Å) at 40 kV and 15 mA for a scan range 2θ=5–90° at a step rate of 1°/min. Coherent crystal length (crystallite size) was estimated through the Scherrer equation (Patterson, 1939) applied to (104) and (200) main Bragg reflection peaks for $CaCO_3$ and CaO, respectively. Peak profiles were fitted using a split pseudo-Voight function to correct for peak widths. Instrumental peak broadening was determined using the NIST SRM 660 LaB_6 standard. PDXL2 Rigaku data analysis software was employed to this end. Scanning electron micrographs were acquired using a Hitachi S4800 SEM-FEG microscope.

Particle size distributions (PSDs) were measured by means of laser diffractometry using a Mastersizer 3000 (Malvern) apparatus. In these tests, the samples were previously dispersed in 2-propanol (as recommended for Ca-based materials according to ISO 14887 (2000)) and sonicated for 30 s to loosen particle aggregates.

Nitrogen adsorption-desorption isotherms were measured at 77 K by means of an ASAP2420 (Micromeritics) instrument. Prior to the analysis, samples were degassed at 350ºC for 8 h. Specific surface area of the samples (S_{BET}) was determined using the BET equation (Brunauer et al., 1938). Total pore volume (Vsp) was calculated from the amount of gas adsorbed at a P/P_0 value of 0.99. Micropore area (St_{micro}) and micropore volume (Vt_{micro}) were estimated from the t-plot method through the Harkins and Jura equation (Harkins and Jura, 1944). Mesopore distributions were obtained by applying the BJH method to the desorption branch of the isotherms (Barrett et al., 1951), and the average pore sizes (wp and wp_{BJH}) were determined by approximating the pore geometry to a cylinder. Wide mesopore and macropore size distributions of calcined samples were analyzed by means of mercury intrusion porosimetry, which was performed using an Autopore IV apparatus (Micromeritics).

3 Results and Discussion

3.a) Materials Characterization

As derived from XRF composition analysis results (Table 1), the calcium carbonate samples employed in the present study contain a very low percentage of impurities. In the case of marble, Mg and Si elements are found in the form of magnesium silicate as was inferred from XRD analysis (Figure 2). The XRD patterns show also a high crystallinity for all the raw samples, with crystallite sizes above the applicability limit of the Scherrer equation (~100 nm).

Table 1. XRF analytical composition of as-received calcium carbonates

(%wt)	**Limestone**	**Chalk**	**Marble**
CaO	55.30	55.72	55.48
MgO	0.20	0.28	0.49
SiO_2	0.29	0.90	0.13
Al_2O_3	0.04	0.48	0.06
Fe_2O_3	0.10	0.26	0.09
K_2O	0.02	0.08	0.02
Na_2O	0.03	ND	ND
P_2O_5	0.04	0.28	ND
MnO	0.03	ND	ND
SO_3	0.04	0.03	0.02

ND : Non detected

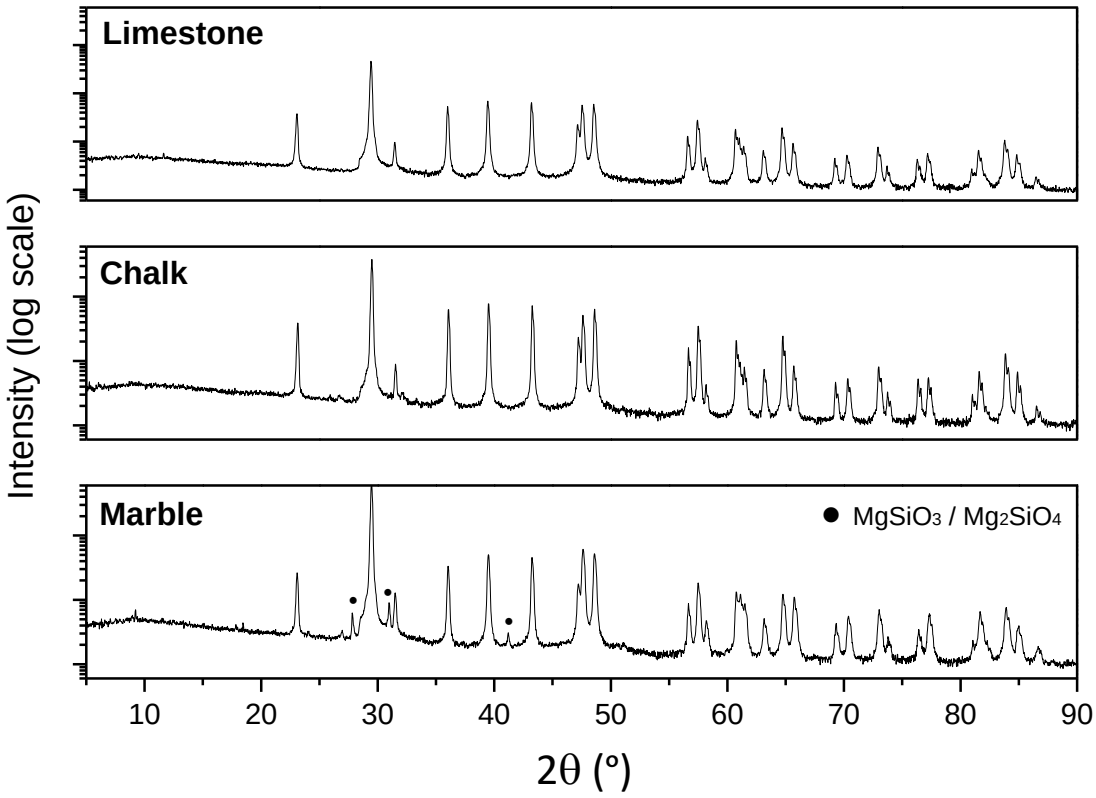

Figure 2. X-ray powder diffractograms of as-received calcium carbonate samples. Intensities are shown in log scale (60-60000 counts range).

As revealed by SEM micrographs (Figure 3), the particles of the different carbonates exhibit diverse morphologies. Thus, limestone is characterized by the presence of small and rounded particles (Fig. 3a), chalk particles show the typical of calcite rhombohedral crystal structure (Fig. 3b), and marble particles are highly heterogeneous with the presence of both very fine particles and polygonal shape bigger ones (Fig. 3c). As will be seen, these observations are consistent with the results derived from laser diffraction particle size analysis. In addition, these micrographs suggest that marble and chalk have higher crystallinity than limestone although their crystallite size cannot be estimated from the Scherrer formula to confirm this observation.

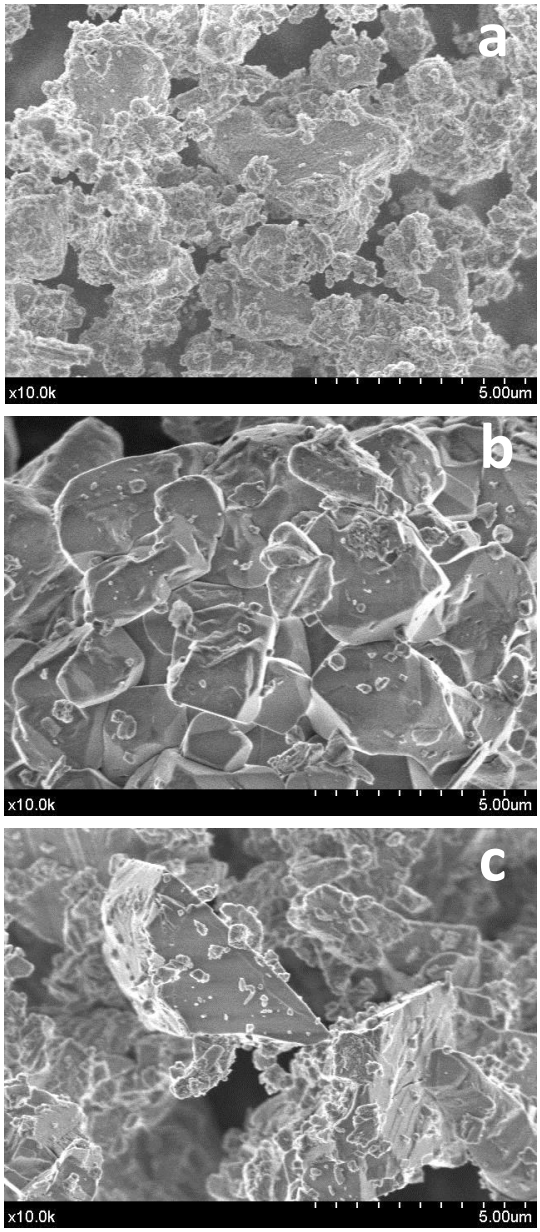

Figure 3. SEM micrographs of limestone (a), chalk (b) and marble (c) samples used in this work.

PSDs (Figure 4) show that the range of particle sizes of the samples is between 0.1 and 100 microns. The smaller particles are found in the limestone sample whereas marble contains the largest ones. Most relevant PSD statistical parameters are summarized in Table 2. The as-received carbonates present very low specific surface area and low porosity as seen from the data obtained from nitrogen adsorption-desorption isotherms (Table 3).

Table 2: PSD statistical values of limestone, chalk and marble samples used in this work

	Limestone	**Chalk**	**Marble**
Dv (10) μm [a]	1.09	1.85	1.67

Dv (50) μm [b]	3.19	7.12	11.17
Dv (90) μm [c]	9.89	22.73	37.83
D [3;2] μm [d]	2.19	3.89	4.43
D [4;3] μm [e]	4.53	10.07	15.97

223

224 a Particle size limit below which 10% of the particles are found

225 b Mass Median Diameter (MMD).

226 c Particle size limit below which 90% of the particles are found

227 d Surface Weighted Mean or Surface Area Moment Mean Diameter

228 e Volume Weighted Mean or Mass Moment Mean Diameter

229

230 Table 3: Specific surface area and porosity data of as-received calcium carbonate samples, estimated by
231 nitrogen adsorption-desorption analysis.

232

	Limestone	**Chalk**	**Marble**
S_{BET} (m^2/g)	0.88	1.13	0.92
St_{micro} (m^2/g)	0.36	0.07	ND
Vsp (cm^3/g)	0.00214	0.00237	0.00243
Vp_{micro} (cm^3/g)	0.00016	0.00002	ND
Wp (nm) [a]	9.8	8.4	10.6
Wp BJH (nm) [b]	29.9	15.0	18.4

233

234 ND: non detected

235 a Mean pore width, wp = 4V/S

236 b Mean BJH pore width, determined by BJH data (4V/S)

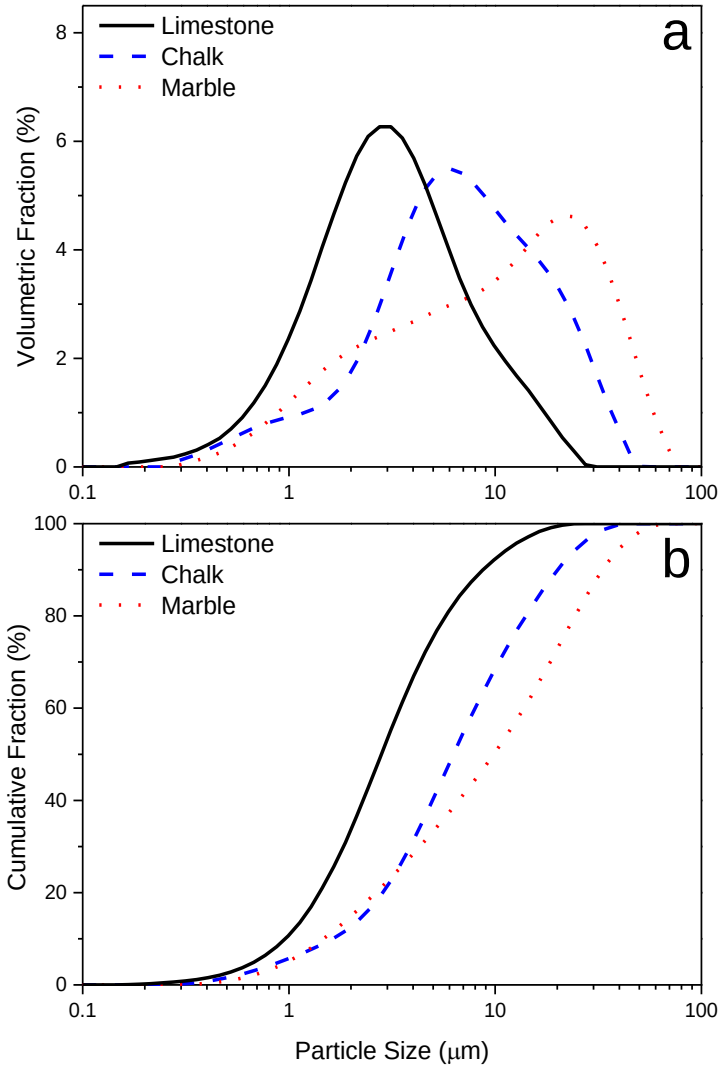

Figure 4: Particle size distributions of limestone, chalk and marble samples as received.

3.b) Multiclycle CaO conversion

The thermograms shown in Figure 5 correspond to the first and last cycles carried out under CaL-CSP storage conditions. As observed in Fig. 5a, the first calcination occurs at a slightly slower rate for marble and chalk as compared to limestone. This observation could be attributed to a larger crystallite size of marble and chalk as was inferred from the SEM analysis, which hinders the diffusion of CO_2 out of the particles as previously reported for limestone samples of diverse crystallinity degree (Valverde et al., 2014). Figure 5 shows that carbonation occurs through two well differentiated phases as widely reported in the literature (Barker, 1973) (Grasa et al., 2009). A first fast reaction controlled phase (FRP), which takes place on the surface of CaO particles, is followed by a much slower diffusion controlled phase (SDP) determined by the counter-current diffusion of CO_3^{2-} cations and O^{2-} anions across the $CaCO_3$

product layer (Bhatia and Perlmutter, 1983) (Sun et al., 2012). As seen in Figure 5, the major contribution to the overall carbonation under CaL-CSP storage conditions occurs in the FRP due to the high CO_2 concentration and carbonation temperature which enhances the kinetics of this phase. Fig. 5a shows that CaO conversion and the reaction kinetics in the first carbonation stage are very similar for the different calcium carbonates. However, CaO deactivation after 20 cycles occurs at diverse degrees for the different carbonates as seen in Fig. 5b. Thus, deactivation is more significant for marble, followed by chalk, while limestone presents the lowest deactivation.

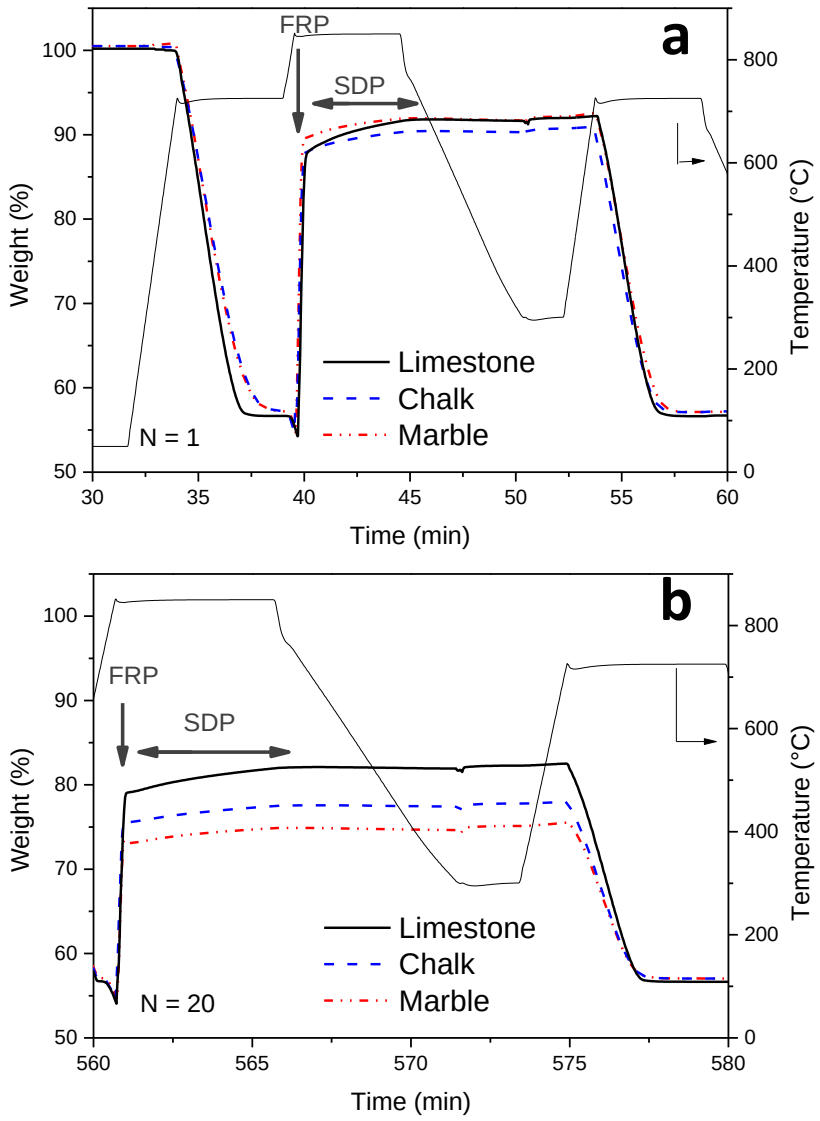

Figure 5. Time evolution of temperature and sample weight for the first (N=1) calcination/carbonation cycle (a) and the last N=20 cycle (b). The fast reaction controlled phase (FRP) and solid-state diffusion controlled phase (SDP) are indicated.

Figure 6 shows multicycle CaO conversion data obtained from the TGA tests carried out under CaL-CSP storage and CO_2 capture conditions for comparison. Conversion at cycle N was calculated as the ratio of the mass of CaO converted to the initial mass of CaO before carbonation m_N:

$$X_N = \frac{m_{carb\,N} - m_N}{m_N} \cdot \frac{56}{44} \quad (2)$$

Where $m_{carb\ N}$ is the sample mass at the end of the carbonation stage. As shown in previous works multicycle conversion data can be generally well fitted by the semi-empirical equation (Valverde, 2013) (Valverde et al., 2013)

$$X_N = X_r + \frac{X_1}{k(N-1)+\left(1-{X_r}/{X_1}\right)^{-1}} \quad (3)$$

where N is the cycle number, X_1 is CaO conversion at the first cycle, k is the deactivation rate constant, and X_r is the residual conversion towards which CaO conversion converges asymptotically after a very large number of cycles. Best fitting parameters k and Xr are shown in Table 5. Even though CaO conversion at the first cycle X_1, is similar for the different calcium carbonates, the deactivation rates under CaL-CSP storage conditions are quite different as was inferred from the thermograms shown in Fig. 5, which leads also to remarkably diverse values of the residual conversion. Thus, the highest residual conversion is obtained for limestone (X_r = 0.51) whereas marble has a residual conversion as low as X_r = 0.27. In contrast with the results obtained under CaL-CSP storage conditions, CaO conversion values derived under CO_2 capture conditions are significantly low (Figure 6b) due to the marked sintering of the CaO particles formed by calcination under high temperature and high CO_2 concentration as widely reported elsewhere (Abanades and Alvarez, 2003) (Alvarez and Abanades, 2005) (Sun et al., 2007). Residual conversions obtained in these conditions are below 0.1 (Table 5) in agreement with reported values in previous works (Abanades and Alvarez, 2003) (Grasa et al., 2008) (Sarrion et al., 2016)(Benitez-Guerrero et al., 2017).

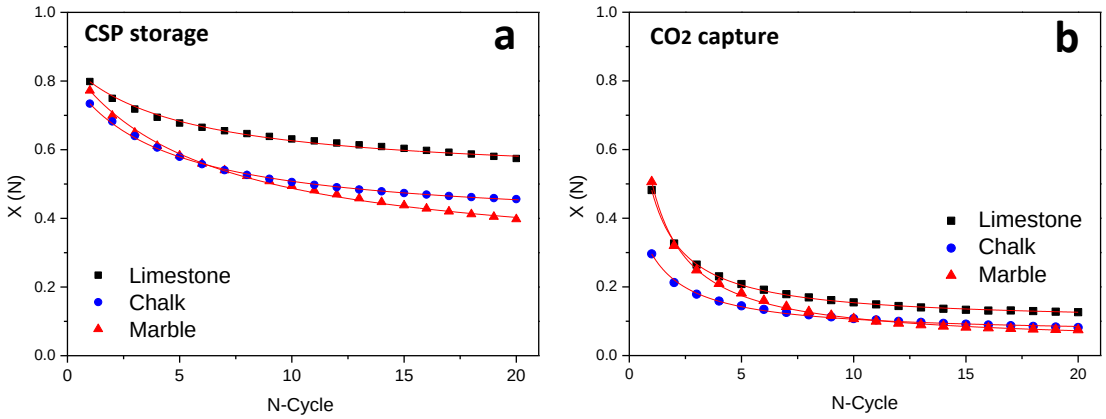

Figure 6. CaO conversion data measured for calcium carbonate samples as a function of the number of carbonation/calcination cycles carried out under CaL-CSP storage conditions (a) and CaL-CO_2 capture conditions (b). The solid lines represent the best fits of Equation (3) to experimental data. Best fitting parameters are shown in Table 5.

Table 5. Best fitting parameters in Eq (2) to CaO conversion data obtained from calcium carbonate samples tested under CaL-CSP storage and CaL-CO_2 capture conditions.

	CaL-CSP storage			**CaL- CO_2 capture**		
	Limestone	**Chalk**	**Marble**	**Limestone**	**Chalk**	**Marble**
k	0.48	0.40	0.22	0.78	0.60	0.63
X_r	0.51	0.38	0.27	0.097	0.061	0.033
R^2	1	0.999	0.997	0.999	0.997	0.998
χ^2	0	6.25E-6	3.57E-5	4.53E-6	8.17E-6	1.79E-5

3.c) Porosimetry analysis

Porosity distributions of samples subjected to just one calcination stage (N=1) and to 6 carbonation/calcination cycles (N=6) in the tubular oven were analyzed by nitrogen adsorption-desorption isotherm and mercury intrusion porosimetry. By using both techniques, a wide range of pore sizes can be analyzed since diverse pore ranges are accessible to N_2 (wide micropores and mesopores) and Hg (essentially meso and macropores).

Main data obtained from these measurements are shown in Table 6. As may be seen, both techniques yield similar values of the surface area and similar pore size distribution profiles (shown in Figure 7). The CaO generated after first calcination of the different calcium carbonates is mainly meso and macroporous, with S_{BET} values close to 20 m^2/g and pore sizes ranging from 10 to 100 nm (peaking at about 40 nm). This nanometric pore range is associated

315 to the intraparticle pores whereas macropores larger than 0.5 μm detected by mercury
316 intrusion correspond to interparticle pores. As would be expected, the specific surface area
317 and pore volume diminish as the number of cycles increases while the pore size distribution
318 shifts towards larger pore sizes as seen in Fig. 7. Thus, according to N_2 physisorption analysis,
319 the surface area reduction (micropores and mesopores range) from the first calcination step
320 (N=1) to the 6^{th}-cycle (N=6) is the highest for CaO derived from chalk (55%) whereas limestone
321 derived CaO shows the lowest reduction (38%). In contrast, this trend is reversed in the large
322 macropores domain according to mercury intrusion measurements. The surface area reduction
323 in this domain is the highest for CaO derived from limestone (53%) whereas marble shows the
324 lowest decrease (37%). The reduction observed in the range of mesopores and smaller
325 macropores (< 100 nm), as depending on the sample type, is consistent with the relative decay
326 of multicycle CaO activity as was observed in Figure 6.
327

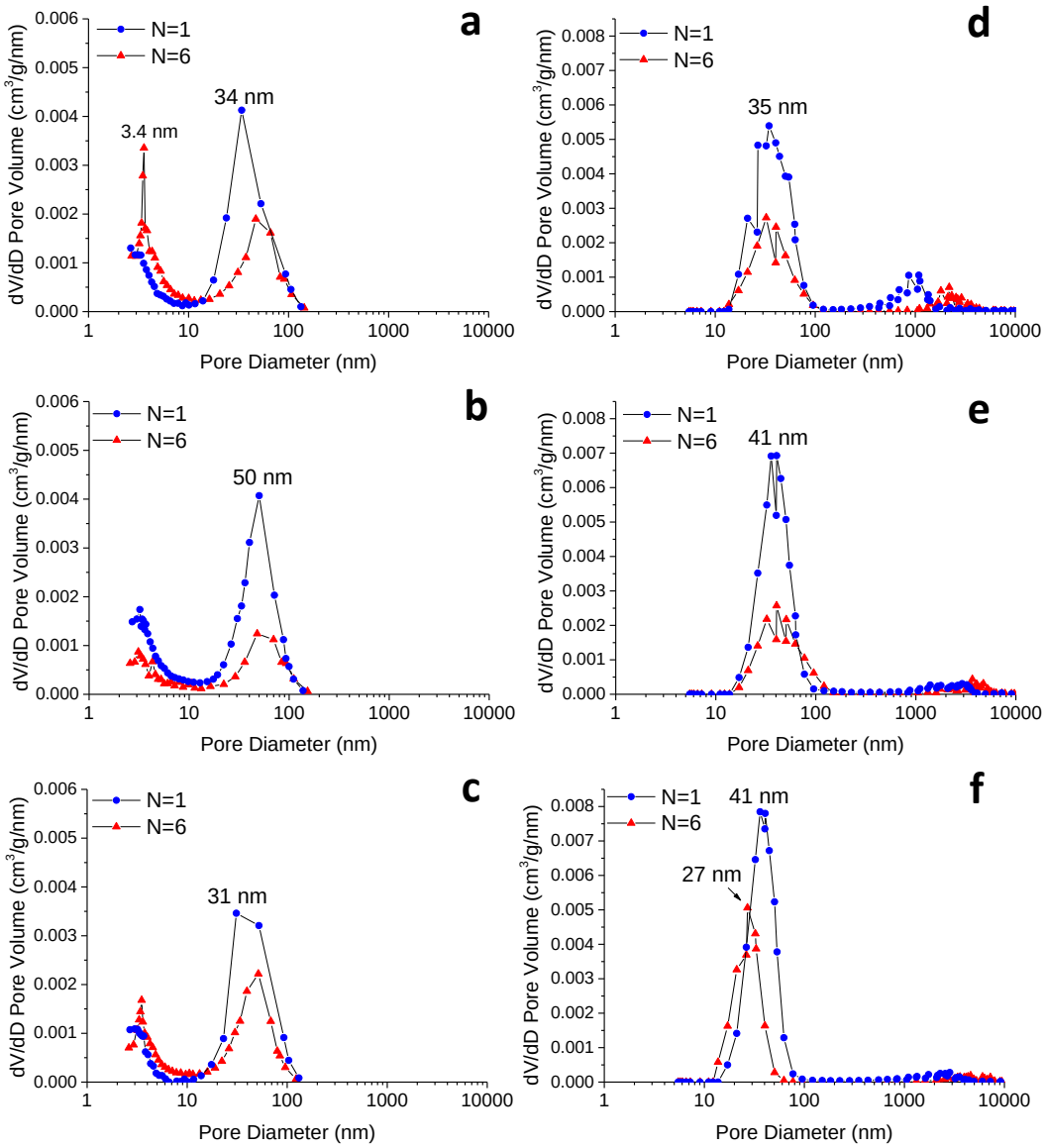

Figure 7. BJH Pore size distributions of CaO derived from limestone (a), chalk (b) and marble (c) after the first and 6th-cycle calcination determined by N_2 physisorption analysis and mercury intrusion porosimetry (d, e, f), for limestone, chalk and marble respectively.

341 Table 6. Specific surface area and porosity data of CaO derived from limestone, chalk and marble after
342 the first (N=1) and 6th-cycle (N=6) calcination obtained from N_2 adsorption-desorption analysis and
343 mercury intrusion porosimetry.
344

N_2 ads-des	**L_cal_1**	**L_cal_6**	**C_cal_1**	**C_cal_6**	**M_cal_1**	**M_cal_6**
S_{BET} (m^2/g)	21	13	20	9	21	11
St_{micro} (m^2/g)	2.9	0.3	1.2	1.3	2.2	0.3
Vsp (cm^3/g)	0.20442	0.11876	0.19850	0.08889	0.23326	0.10871
Vp_{micro} (cm^3/g)	0.00125	0.00002	0.00046	0.00054	0.00099	0.00005
Wp (nm) [a]	38	37	41	41	44	40
Wp BJH (nm) [b]	37	35	40	42	40	36
Hg porosimetry	**L_cal_1**	**L_cal_6**	**C_cal_1**	**C_cal_6**	**M_cal_1**	**M_cal_6**
Pore Area (m^2/g)	26	12	23	12	24	15
Total intrusión Volume (cm^3/g)	1.67	1.36	1.18	1.25	1.16	0.89
Median Pore Diameter (nm) [c]	43	43	43	50	42	30

345 a Mean pore width, wp = 4V/S
346 b Mean BJH pore width, determined by BJH desorption branch data (4V/S)
347 c Calculated at 50% of the total pore area

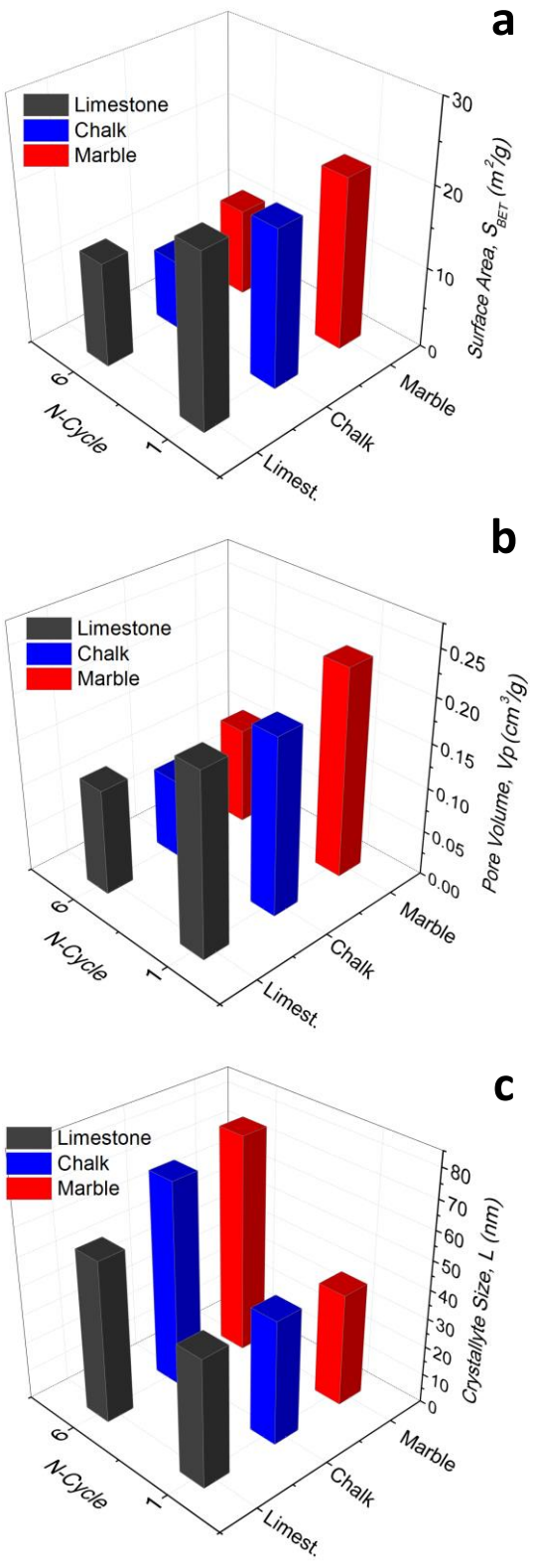

348

349

350 Figure 8. Surface area S_{BET} (c), pore volume (b) and crystallite size (c) for CaO derived from limestone,

351 chalk and marble after the first and 6th-cycle calcination.

352

3.d) Microstructural and morphological characterization

Figures 8a-c show the evolution of surface area, pore volume and crystallite size for the CaO resulting from calcination in the first (N=1) and 6^{th} cycles (N=6) of the different carbonates analyzed. From a microstructural point of view, the increase of CaO crystallite size with the cycle number (shown in the insets of Fig. 9) is consistent with the loss of surface area and pore volume as previously reported for limestone samples subjected to prolonged calcination at diverse conditions of temperature and CO_2 concentration in the calciner environment (Valverde et al., 2015). As a general trend, the size and volume of pores is decreased as the crystallite size increases along the cycles. The growth of CaO crystallite size with the cycle number depends however on the type of calcium carbonate mineral. Although the dimension of the crystallites are around 40 nm after the first calcination for the different starting carbonates, the size increment at the 6^{th}-cycle is larger for the CaO derived from marble (95%), followed by chalk (65%) whereas the lowest degree of crystallite size growth is observed for the CaO derived from limestone (27%). This differentiated crystallite growth among the different carbonates is maintained as the number of cycles is increased as was verified by analyzing the CaO obtained after the 20 cycles carried out in the thermogravimetric analyzer (Fig. 9c).

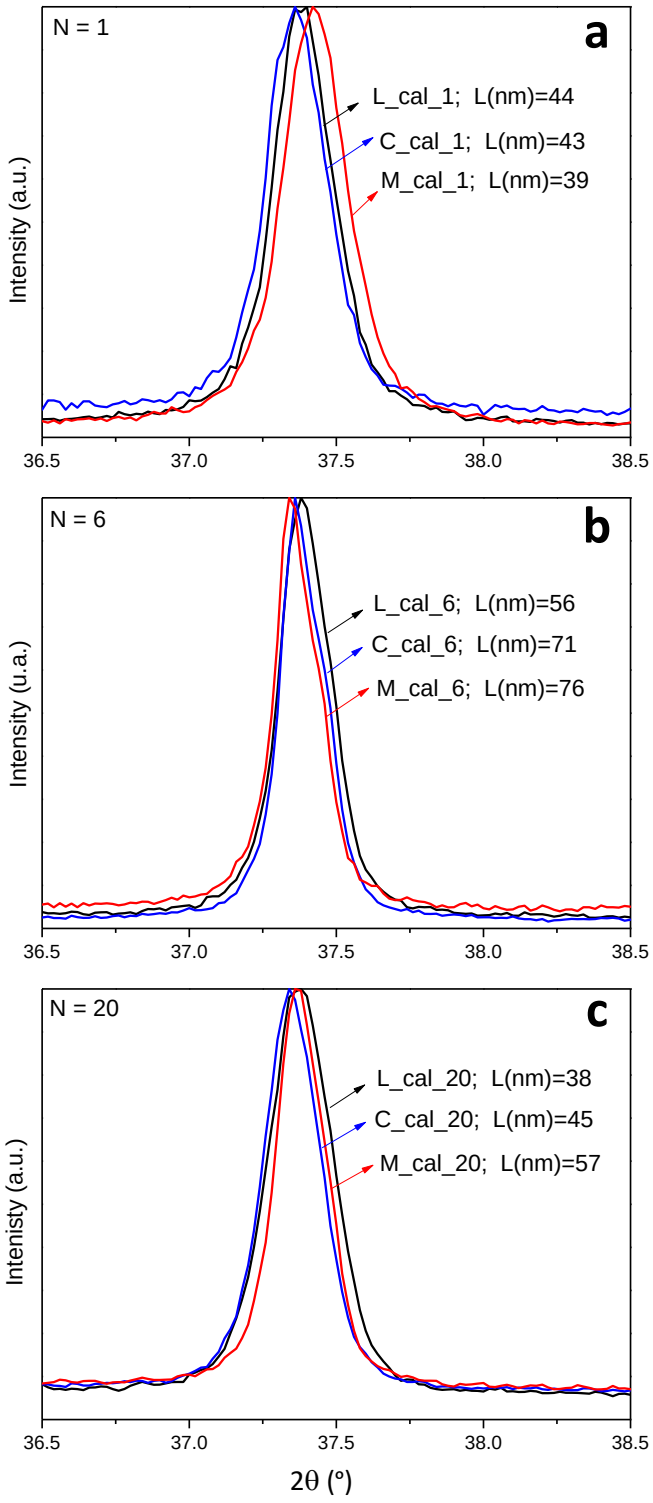

370

371 Figure 9. Normalized X-ray diffractograms showing the main Bragg (200) reflection peak for CaO derived
372 from limestone, chalk and marble, after calcination in the first (a) and sixth (b) cycles (tubular oven) and
373 (c) after 20 cycles in the Q5000IR thermogravimetric analyzer. The insets display the corresponding
374 crystallite sizes, L(nm).

375 The reduced sintering and crystallite size growth exhibited by the CaO derived from
376 limestone is consistent with its lower deactivation as compared to marble and chalk observed
377 from the TGA tests (Fig. 6). On the other hand, it can be argued that the highest increment of
378 CaO specific surface area observed for chalk and the highest increase of CaO crystallite size
379 shown by marble would yield compensating effects on their carbonation reactivity, which
380 would lead to the similar deactivation observed for both minerals (Figure 6).

381 Morphological changes of the CaO obtained after different number of cycles were
382 analyzed by SEM. As seen in low magnification SEM pictures (Fig. 10), the CaO particles inherit
383 the morphology of the parent calcium carbonates. As the number of carbonation/calcination
384 cycles increases, CaO sintering becomes apparent as shown in Figure 10 where "bottlenecks"
385 formed by the coalescence of CaO grains can be seen. Agglomeration and growth of the CaO
386 grains become clearly visible at higher magnifications (Fig. 11); however, the typical rod-
387 shaped arrangement of CaO grains with cylindrical pores reported in previous works
388 (Abanades and Alvarez, 2003)(Rodriguez-Navarro et al., 2009) is not appreciated on the
389 external surface of CaO particles shown in Figure 11. The size and morphology of CaO grains
390 observed in these SEM pictures on the external surface of the CaO particles, after the first and
391 6^{th}-cycles, differ as depending on the nature of the starting calcium carbonate. Thus, CaO
392 grains appear more rounded for the CaO derived from limestone (Fig. 11a) and more
393 elongated for chalk and marble derived CaO (Fig. 11c and f, respectively). SEM pictures of the
394 samples derived after the 20 cycles are shown in Fig. 12. Arguably, the more elongated the
395 CaO grains, the larger the surface contact area between them, which will favor crystallite
396 growth and pore volume reduction as was inferred from XRD and physisorption analysis.

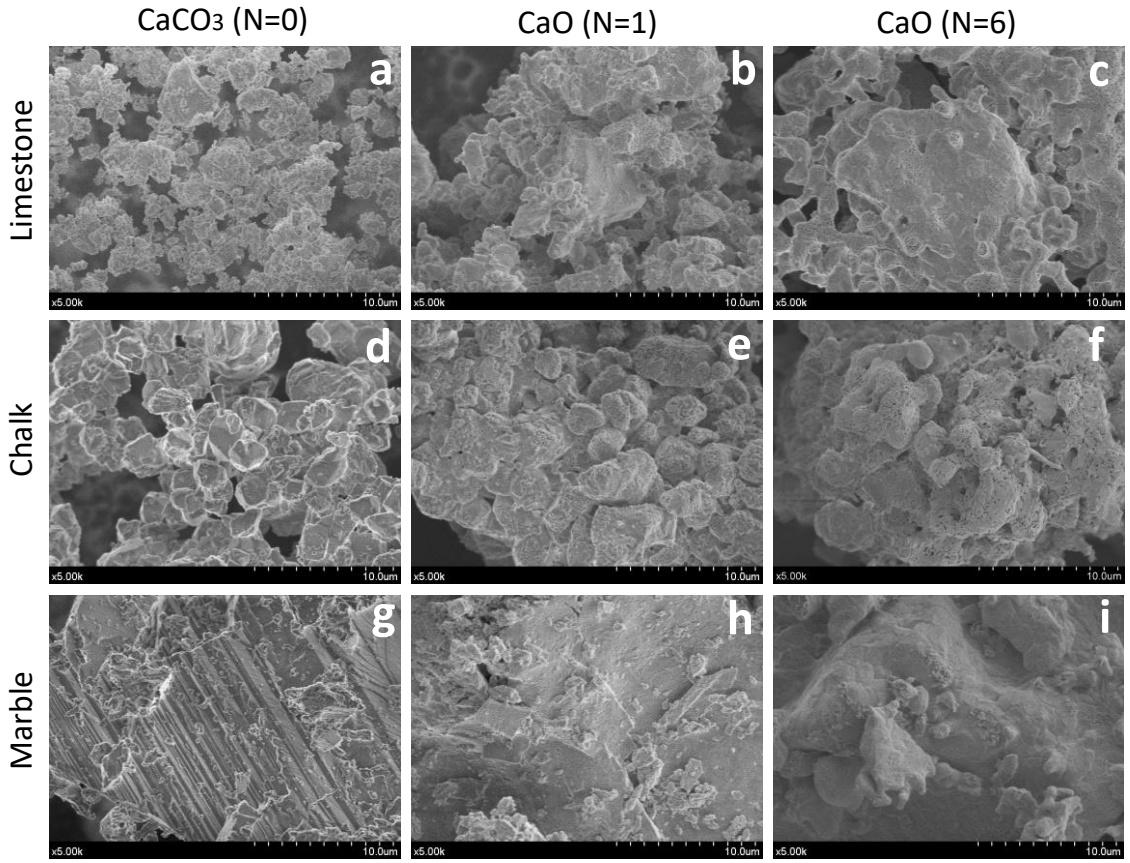

Figure 10. SEM micrographs for limestone (a), chalk (d) and marble (g) samples and for CaO derived from them after the first calcination step, L_cal_1 (b), C_cal_1 (e) and M_cal_1 (h), and after the 6th-cycle, L_cal_6 (c), C_cal_6 (f) and M_cal_6 (i). (Magnification 5000x).

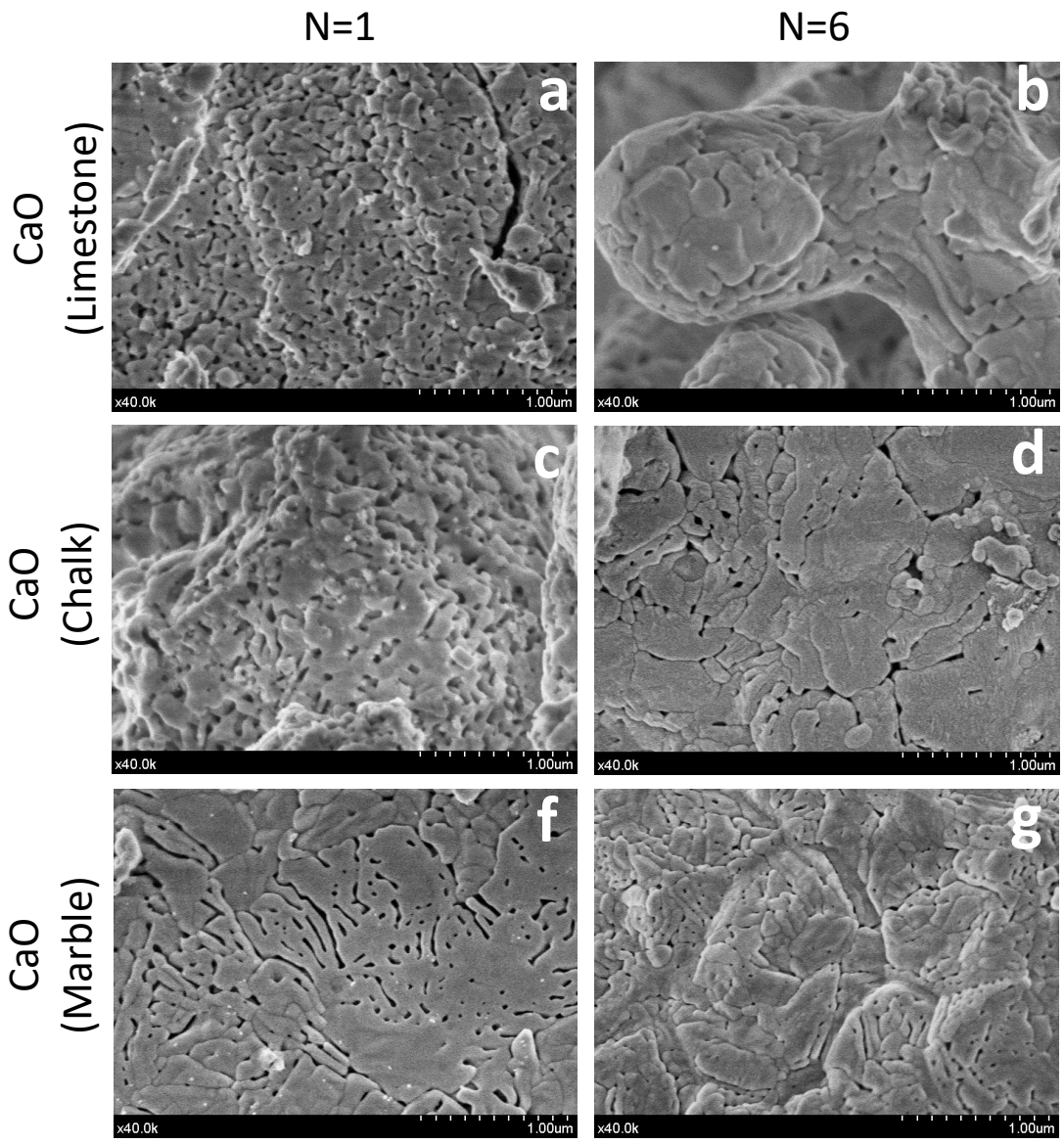

401

402 Figure 11. SEM micrographs of CaO derived from limestone, chalk and marble obtained after the first
403 calcination step, L_cal_1 (a), C_cal_1 (c) and M_cal_1 (f), and after the 6th-cycle, L_cal_6 (b), C_cal_6 (d)
404 and M_cal_6 (g). (Magnification 40000x).

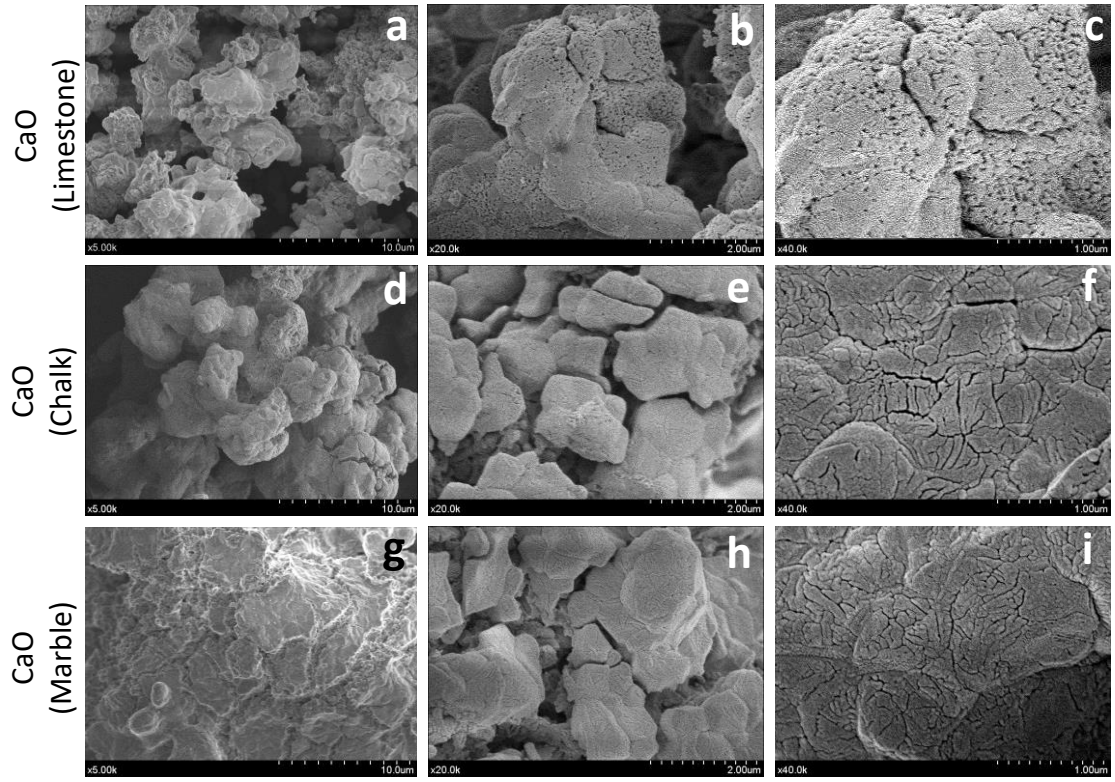

Figure 12. SEM micrographs at different magnifications of CaO particles derived from limestone (first row), chalk (second row) and marble (third row) obtained in the Q5000IR thermogravimetric analyzer after the 20thcycle.

Figure 13 show SEM pictures of samples obtained by breaking the CaO particles resulting after the cycles, which leaves exposed the interior skeleton of these particles. As may be seen, a highly sintered CaO layer is built upon the particle's surface whereas the interior of the particles exhibit a relatively more porous CaO skeleton. These SEM pictures suggest that the access of CO_2 to this porous CaO inner skeleton is blocked by the $CaCO_3$ layer generated in the carbonation stage of the cycles. Therefore, the carbonation/calcination reaction would be carried out only at the external surface of the particles. Pore plugging would enhance further CaO deactivation as particle size is increased. As seen in Fig.14, the residual conversion Xr values obtained from the TGA analysis (Table 5) scale inversely with the initial size of the particles for the threes carbonates tested. The larger the calcium carbonate particles the lower Xr is. The favorable carbonation conditions (high temperature and high CO_2 concentration) would lead to a quick built up of the $CaCO_3$ layer, which in addition may grow up to a large thickness (Li et al., 2012), therefore promoting pore plugging. Thus, although the mild calcinations carried out at CaL conditions for CSP storage would lead to a relatively porous CaO

skeleton with a high surface area available for reaction, pore plugging would pose a serious limit to carbonation.

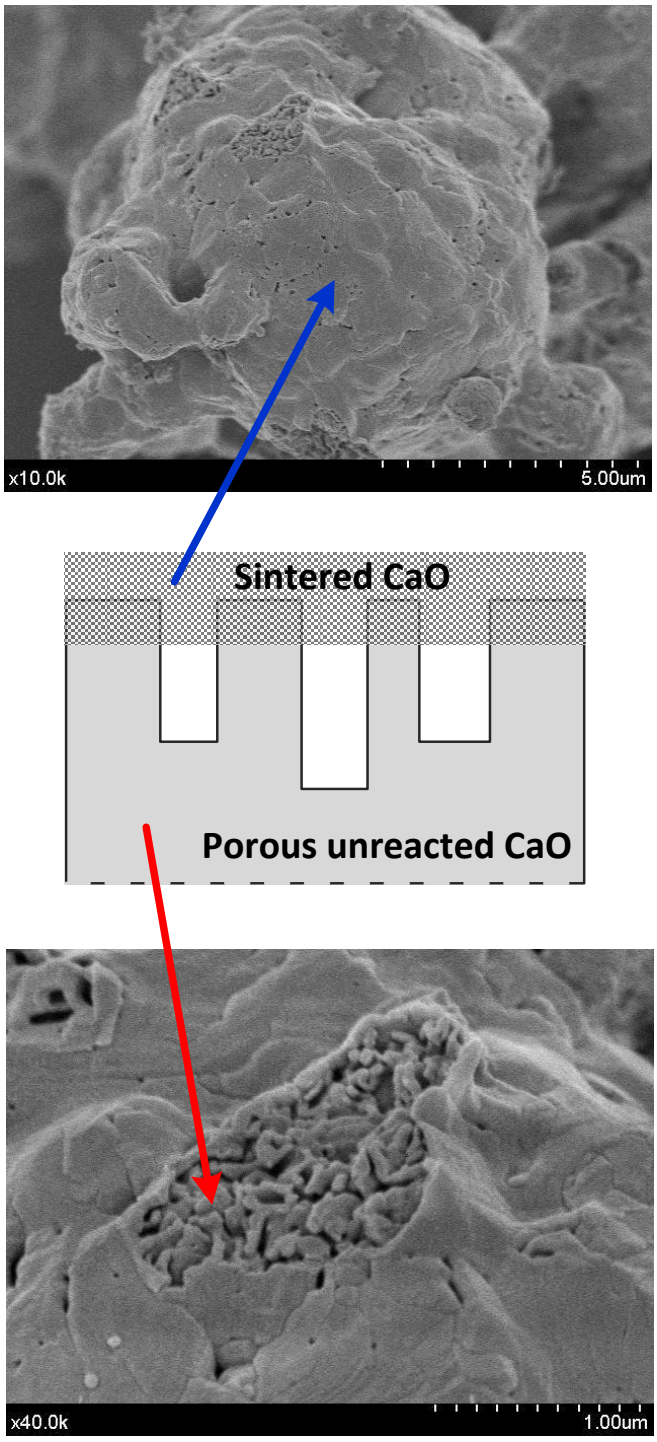

Figure 13. SEM pictures showing a superficial CaO layer sintered after several calcination/carbonation cycles and an inner porous CaO that remains unreacted after the cycles due to pore plugging.

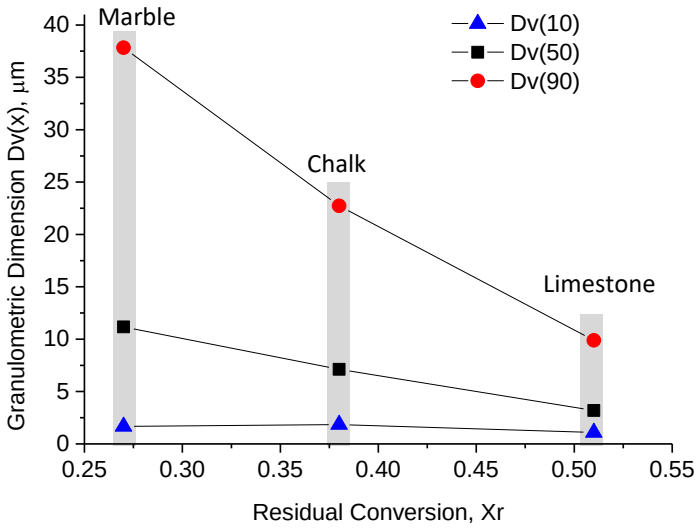

Figure 14. Particle size distribution parameters Dv(10), Dv(50) and Dv(90) of the starting calcium carbonates versus residual CaO conversion values derived from multicycle TGA tests carried out under CaL-CSP storage conditions.

Conclusions

This work analyzes the multicycle activity of CaO derived from diverse natural $CaCO_3$ minerals (limestone, chalk and marble) at optimum Calcium-Looping conditions for the thermochemical storage of energy in Concentrated Solar Power plants. CaO deactivation with the number of cycles is correlated to the growth of crystallite size and the corresponding decrease of CaO porosity. Under these conditions, mild calcination (relatively low temperature in the absence of CO_2) would lead to a highly porous CaO skeleton with a high surface area available for fast carbonation. However, the favorable carbonation environment (high temperature under high CO_2 concentration) would lead to a very quick formation of a thick $CaCO_3$ layer on the surface of the particles, which would block the access of CO_2 to the porous CaO inner skeletons. Thus, pore plugging has been identified as a main limiting factor for the multicycle CaO activity. Remarkably, this phenomenon is observed in our work to occur for relatively small size particles and would be promoted even further for larger particles (above ~100 µm) as needed in practice. In order to use $CaCO_3$ natural minerals for thermochemical energy storage in CSP plants strategies should be therefore devised in future works with a main focus on avoiding pore plugging.

Acknowledgements

Financial support by the Spanish Government Agency Ministerio de Economia y Competitividad (contracts CTQ2014-52763-C2-2-R and CTQ2014-52763-C2-1-R) is acknowledged. The authors gratefully acknowledge Omya Clariana and Segura S.L. companies for supplying us with the materials used in our study. We acknowledge the Functional Characterization services of Innovation, Technology and Research Center of the University of Seville (CITIUS) and University of Málaga (SCAI).

References

2000. ISO 14887: Sample preparation—Dispersing procedures for particles in liquids, in: ISO (Ed.). Genève

Abanades, J.C., Alvarez, D., 2003. Conversion limits in the reaction of CO_2 with lime. Energy and Fuels 17(2), 308-315.

Alvarez, D., Abanades, J.C., 2005. Pore-size and shape effects on the recarbonation performance of calcium oxide submitted to repeated calcination/recarbonation cycles. Energy & Fuels 19(1), 270-278.

Arias, B., Diego, M.E., Abanades, J.C., Lorenzo, M., Diaz, L., Martínez, D., Alvarez, J., Sánchez-Biezma, A., 2013. Demonstration of steady state CO_2 capture in a 1.7 MWth calcium looping pilot. International Journal of Greenhouse Gas Control 18, 237-245.

Ávila-Marín, A.L., 2011. Volumetric receivers in Solar Thermal Power Plants with Central Receiver System technology: A review. Solar Energy 85(5), 891-910.

Barker, R., 1973. The reversibility of the reaction $CaCO_3 \rightleftarrows CaO+CO_2$. Journal of Applied Chemistry and Biotechnology 23(10), 733-742.

Barker, R., 1974. The reactivity of calcium oxide towards carbon dioxide and its use for energy storage. Journal of Applied Chemistry and Biotechnology 24(4-5), 221-227.

Barrett, E.P., Joyner, L.G., Halenda, P.P., 1951. The determination of pore volume and area distributions in porous substances. I. Computations from nitrogen isotherms. Journal of the American Chemical Society 73(1), 373-380.

Behar, O., Khellaf, A., Mohammedi, K., 2013. A review of studies on central receiver solar thermal power plants. Renewable and Sustainable Energy Reviews 23, 12-39.

Benitez-Guerrero, M., Sarrion, B., Perejon, A., Sanchez-Jimenez, P.E., Perez-Maqueda, L., Valverde, J.M., 2017. Large-scale high-temperature solar energy storage using natural minerals. Solar Energy Materials and Solar Cells, 168, 14-21.

Berger, E.E., 1927. Effect of steam on the decomposition of limestone. Industrial & Engineering Chemistry 19(5), 594-596.

Beruto, D.T., Botter, R., Cabella, R., Lagazzo, A., 2010. A consecutive decomposition–sintering dilatometer method to study the effect of limestone impurities on lime microstructure and its water reactivity. Journal of the European Ceramic Society 30(6), 1277-1286.

Bhatia, S.K., Perlmutter, D.D., 1983. Effect of the product layer on the kinetics of the CO_2-lime reaction. AIChE Journal 29(1), 79-86.

Blamey, J., Anthony, E.J., Wang, J., Fennell, P.S., 2010. The calcium looping cycle for large-scale CO_2 capture. Progress in Energy and Combustion Science 36(2), 260-279.

Brunauer, S., Emmett, P.H., Teller, E., 1938. Adsorption of gases in multimolecular layers. Journal of the American Chemical Society 60(2), 309-319.

Coppola, A., Scala, F., Itskos, G., Grammelis, P., Pawlak-Kruczek, H., Antiohos, S.K., Salatino, P., Montagnaro, F., 2013. Performance of natural sorbents during Calcium Looping cycles: A comparison between fluidized bed and thermo-gravimetric tests. Energy & Fuels 27(10), 6048-6054.

Cormos, A.-M., Simon, A., 2015. Assessment of CO_2 capture by calcium looping (CaL) process in a flexible power plant operation scenario. Applied Thermal Engineering 80, 319-327.

Cot-Gores, J., Castell, A., Cabeza, L.F., 2012. Thermochemical energy storage and conversion: A-state-of-the-art review of the experimental research under practical conditions. Renewable and Sustainable Energy Reviews 16(7), 5207-5224.

Cussler, E.L., 1997. Diffusion: Mass Transfer in Fluid Systems. Cambridge University Press.

Chacartegui, R., Alovisio, A., Ortiz, C., Valverde, J.M., Verda, V., Becerra, J.A., 2016. Thermochemical energy storage of concentrated solar power by integration of the calcium looping process and a CO_2 power cycle. Applied Energy 173, 589-605.

Dieter, H., Hawthorne, C., Zieba, M., Scheffknecht, G., 2013. Progress in Calcium Looping post combustion CO_2 capture: Successful pilot scale demonstration. Energy Procedia 37, 48-56.

Ebrahimi, H., Rahmani, M., 2016. A new design for CO_2 capture and usage in a syngas production unit by carbonate chemical looping. Journal of Natural Gas Science and Engineering 36, Part A, 241-251.

Erans, M., Manovic, V., Anthony, E.J., 2016. Calcium looping sorbents for CO_2 capture. Applied Energy 180, 722-742.

Fennell, P.S., Pacciani, R., Dennis, J.S., Davidson, J.F., Hayhurst, A.N., 2007. The effects of repeated cycles of calcination and carbonation on a variety of different limestones, as measured in a hot fluidized bed of sand. Energy & Fuels 21(4), 2072-2081.

Fernández, A.G., Ushak, S., Galleguillos, H., Pérez, F.J., 2014. Development of new molten salts with $LiNO_3$ and $Ca(NO_3)_2$ for energy storage in CSP plants. Applied Energy 119, 131-140.

Flamant, G., Hernandez, D., Bonet, C., Traverse, J.-P., 1980. Experimental aspects of the thermochemical conversion of solar energy; Decarbonation of $CaCO_3$. Solar Energy 24(4), 385-395.

Grasa, G., Murillo, R., Alonso, M., Abanades, J.C., 2009. Application of the random pore model to the carbonation cyclic reaction. AIChE Journal 55(5), 1246-1255.

Grasa, G.S., Abanades, J.C., Alonso, M., González, B., 2008. Reactivity of highly cycled particles of CaO in a carbonation/calcination loop. Chemical Engineering Journal 137(3), 561-567.

Hanak, D.P., Anthony, E.J., Manovic, V., 2015. A review of developments in pilot-plant testing and modelling of calcium looping process for CO_2 capture from power generation systems. Energy & Environmental Science 8(8), 2199-2249.

Harkins, W.D., Jura, G., 1944. Surfaces of Solids. XIII. A Vapor adsorption method for the determination of the area of a solid without the assumption of a molecular area, and the areas occupied by nitrogen and other molecules on the surface of a solid. Journal of the American Chemical Society 66(8), 1366-1373.

Hinkley, J.T., Hayward, J.A., Curtin, B., Wonhas, A., Boyd, R., Grima, C., Tadros, A., Hall, R., Naicker, K., 2013. An analysis of the costs and opportunities for concentrating solar power in Australia. Renewable Energy 57, 653-661.

Li, Y., Zhao, C., Chen, H., Liu, Y., 2009. Enhancement of Ca-based sorbent multicyclic behavior in Ca looping process for CO_2 separation. Chemical Engineering & Technology 32(4), 548-555.

Li, Z.-s., Fang, F., Tang, X.-y., Cai, N.-s., 2012. Effect of temperature on the carbonation reaction of CaO with CO_2. Energy & Fuels 26(4), 2473-2482.

Lu, D.Y., Hughes, R.W., Anthony, E.J., 2008. Ca-based sorbent looping combustion for CO_2 capture in pilot-scale dual fluidized beds. Fuel Processing Technology 89(12), 1386-1395.

Martínez, I., Grasa, G., Murillo, R., Arias, B., Abanades, J.C., 2012. Kinetics of calcination of partially carbonated particles in a Ca-Looping system for CO_2 capture. Energy & Fuels 26(2), 1432-1440.

N'Tsoukpoe, K.E., Liu, H., Le Pierrès, N., Luo, L., 2009. A review on long-term sorption solar energy storage. Renewable and Sustainable Energy Reviews 13(9), 2385-2396.

Pacciani, R., Müller, C.R., Davidson, J.F., Dennis, J.S., Hayhurst, A.N., 2010. The performance of a novel synthetic Ca-based solid sorbent suitable for the removal of CO_2 and SO_2 from flue

555 gases in a fluidised bed, in: Yue, G., Zhang, H., Zhao, C., Luo, Z. (Eds.), Proceedings of the 20th
556 International Conference on Fluidized Bed Combustion. Springer Berlin Heidelberg, Berlin,
557 Heidelberg, pp. 972-978.
558 Pardo, P., Deydier, A., Anxionnaz-Minvielle, Z., Rougé, S., Cabassud, M., Cognet, P., 2014. A
559 review on high temperature thermochemical heat energy storage. Renewable and Sustainable
560 Energy Reviews 32, 591-610.
561 Patterson, A.L., 1939. The Scherrer formula for X-ray particle size determination. Physical
562 Review 56(10), 978-982.
563 Perejón, A., Romeo, L.M., Lara, Y., Lisbona, P., Martínez, A., Valverde, J.M., 2016. The Calcium-
564 Looping technology for CO_2 capture: On the important roles of energy integration and sorbent
565 behavior. Applied Energy 162, 787-807.
566 Pinheiro, C.I.C., Fernandes, A., Freitas, C., Santos, E.T., Ribeiro, M.F., 2016, Waste marble
567 powders as promising inexpensive natural CaO-based sorbents for post-combustion CO_2
568 capture. Industrial & Engineering Chemistry Research 55, 7860-7872.
569 Prieto, C., Cooper, P., Fernández, A.I., Cabeza, L.F., 2016. Review of technology:
570 Thermochemical energy storage for concentrated solar power plants. Renewable and
571 Sustainable Energy Reviews 60, 909-929.
572 Rodriguez-Navarro, C., Ruiz-Agudo, E., Luque, A., Rodriguez-Navarro, A.B., Ortega-Huertas, M.,
573 2009. Thermal decomposition of calcite: Mechanisms of formation and textural evolution of
574 CaO nanocrystals. American Mineralogist 94(4), 578-593.
575 Sarrion, B., Valverde, J.M., Perejon, A., Perez-Maqueda, L., Sanchez-Jimenez, P.E., 2016. On the
576 multicycle activity of natural limestone/dolomite for thermochemical energy storage of
577 concentrated solar power. Energy Technology 4(8), 1013-1019.
578 Siva Reddy, V., Kaushik, S.C., Ranjan, K.R., Tyagi, S.K., 2013. State-of-the-art of solar thermal
579 power plants—A review. Renewable and Sustainable Energy Reviews 27, 258-273.
580 Stanmore, B.R., Gilot, P., 2005. Review—calcination and carbonation of limestone during
581 thermal cycling for CO_2 sequestration. Fuel Processing Technology 86(16), 1707-1743.
582 Ströhle, J., Junk, M., Kremer, J., Galloy, A., Epple, B., 2014. Carbonate looping experiments in a
583 1 MWth pilot plant and model validation. Fuel 127, 13-22.
584 Sun, P., Grace, J.R., Lim, C.J., Anthony, E.J., 2007. The effect of CaO sintering on cyclic CO_2
585 capture in energy systems. AIChE Journal 53, 2432-2442.
586 Sun, P., Grace, J.R., Lim, C.J., Anthony, E.J., 2008. Investigation of attempts to improve cyclic
587 CO_2 capture by sorbent hydration and modification. Industrial & Engineering Chemistry
588 Research 47(6), 2024-2032.

589 Sun, Z., Luo, S., Qi, P., Fan, L.-S., 2012. Ionic diffusion through Calcite ($CaCO_3$) layer during the
590 reaction of CaO and CO_2. Chemical Engineering Science 81, 164-168.
591 Taketomo, E., Fujiura, M., 1984. Porous materials for concentration and separation of
592 hydrogen or helium, and process therewith for the separation of the gas. Google Patents.
593 Valverde, J.M., 2013. A model on the CaO multicyclic conversion in the Ca-looping process.
594 Chemical Engineering Journal 228, 1195-1206.
595 Valverde, J.M., Sanchez-Jimenez, P.E., Perejon, A., Perez-Maqueda, L.A., 2013. CO_2 multicyclic
596 capture of pretreated/doped CaO in the Ca-looping process. Theory and experiments. Physical
597 Chemistry Chemical Physics 15(28), 11775-11793.
598 Valverde, J.M., Sanchez-Jimenez, P.E., Perez-Maqueda, L.A., 2014. Effect of heat
599 pretreatment/recarbonation in the Ca-Looping process at realistic calcination conditions.
600 Energy & Fuels 28(6), 4062-4067.
601 Valverde, J.M., Sanchez-Jimenez, P.E., Perez-Maqueda, L.A., 2015. Limestone calcination
602 nearby equilibrium: Kinetics, CaO crystal structure, sintering and reactivity. The Journal of
603 Physical Chemistry C 119(4), 1623-1641.
604 Wdowin, M., Franus, W., Panek, R., 2012. Preliminary results of usage possibilites of carbonate
605 and zeolitic sorbents in CO_2 capture. Fresenius Environmental Bulletin 21(12) 3726-3734
606 Zhang, H.L., Baeyens, J., Degrève, J., Cacères, G., 2013. Concentrated solar power plants:
607 Review and design methodology. Renewable and Sustainable Energy Reviews 22, 466-481.